CHALMERS

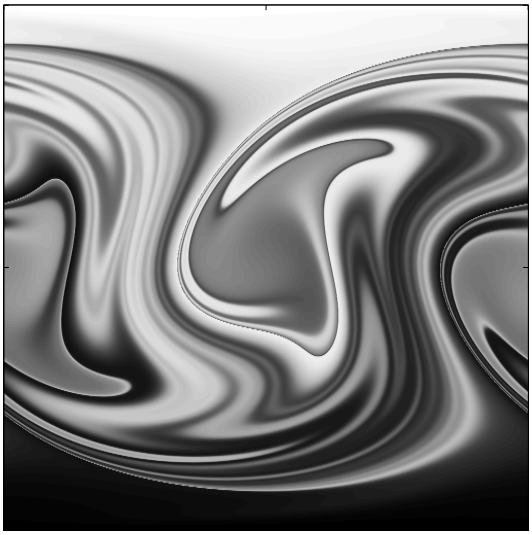

# Rényi entropy and finite Lyapunov exponents as metrics of transport and mixing in an idealised stratosphere

*Master's of Science Thesis*

JAKOB GRAHN

Department of Earth and Space Sciences
Chalmers University of Technology
Gothenburg, Sweden 2012



Supervisor:
Dr. Adrian McDonald
Department of Physics and Astronomy,
University of Canterbury,
Christchurch, New Zealand
Phone: +64 3 364-2281
Email: adrian.mcdonald@canterbury.ac.nz

Examiner:
Prof. Donal Murtagh
Department of Earth and Space Sciences,
Chalmers University of Technology,
Gothenburg, Sweden
Phone: +46 31 772 56 51
Email: donal.murtagh@chalmers.se

Cover figure:
A simulated tracer field produced during the thesis work.

**Abstract**

Most numerical metrics for diagnosing transport and mixing in fluid flows are based on calculating trajectories and thus knowing the velocity fields of the flows. Velocity fields are however difficult to measure globally on Earth. Tracer fields are on the other hand easier to measure and tracer based metrics could therefore prove to be valuable. A newly proposed metric based on the Rényi entropy of tracer values is examined. Although the metric has been used before, the exact theoretical connection to transport and mixing appears to be unclear to us. This motivates us to examine the metric under controlled circumstances. A simple model, defined by only a few parameters, is implemented and used as a test bench for comparing the metric with conventional trajectory based metrics. In particular, the finite time and the finite size Lyapunov exponents are considered for the comparison. We show that the Rényi entropy metric features the main transport barriers of the model and a positive correlation to the finite Lyapunov exponents is found.

# Acknowledgements

My sincere thanks goes to my supervisor Dr. Adrian McDonald for giving me the opportunity to work on this project, visit New Zealand and also letting me attend the European Geosciences Union General Assembly 2012, in Vienna. My thanks also goes to Donal Murtagh as my examiner at Chalmers.

I would further like to give my appreciation to the members of the Atmospheric physics group at University of Canterbury, for help with things like technicalities in Matlab to finding the right bicycle shop in Christchurch. I am also very grateful for the head clearing weekend hikes with Richard Kimberly, Bryce Williamson and the others at Christchurch tramping club.

Further thanks goes to Ångpanneföreningen's Foundation for Research and Development and Anna Whitlocks Minnesfond for the financial support in terms of scholarships, making the stay in New Zealand possible.

Finally, I'd like to give my warmest thanks to my brother and my parents for all the inspiration and for always standing by me.

Jakob Grahn, Christchurch New Zealand, 2 March, 2012

# Contents

# 1

# Introduction

Transport and mixing of fluids is an important topic in a wide range of fields in science and technology. It relates to fusion energy, chemical reactors, aeronautics, combustion, agricultural engineering and polymer processing just to mention a few. At present, it seems as if many problems in the atmospheric sciences are related to transport and mixing in one way or the other as well. The stratosphere is of particular importance in this respect. Characterised by large scale horizontal advection, it plays a central role the distribution of chemical species globally. Good ways of quantifying the amount of which fluids are transported and mixed are therefore valuable.

This thesis is concerned with the assessment of a newly proposed tracer based metric (Krützmann et al., 2008) and its usefulness to quantify transport and mixing in stratospheric flows is examined. It is based on the so called *Rényi entropy* (RE) of tracer fields. The Rényi entropy is a complexity measure of probability distributions and the main inspiration for its use on tracer data comes from Sparling (2000). Other ways of using the *Shannon entropy*, which is a special case of the Rényi entropy, has also been used for diagnosing mixing by, for example, Camesasca et al. (2006) and Guida et al. (2010).

Although Rényi entropy has been used before as a metric of transport and mixing, we are not aware of the exact theoretical connection to these processes. This motivates us to test the metric under controlled circumstances. In particular, a previously studied flow model (Shuckburgh and Haynes, 2003) defined by only a few parameters is adopted. Despite the simplicity of the model, it possesses the main dynamical characteristics of the stratosphere. Two widely used trajectory based metrics, the *finite time Lyapunov exponents* (FTLE) and the *finite size Lyapunov exponents* (FSLE), are further considered (Boffetta et al., 2001; Bowman, 1993; Garny et al., 2007; McKenna et al., 2000; Pierrehumbert and Yang, 1992).

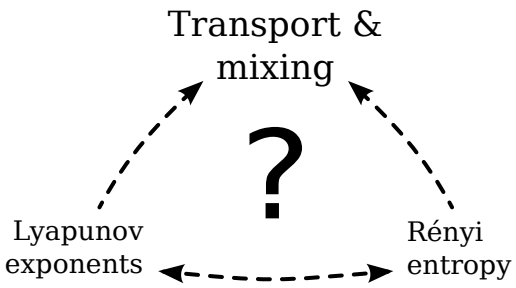


**Figure 1.1:** The main goal of this thesis is to evaluate if the proposed Rényi entropy metric can be used as a diagnostic for stratospheric transport and mixing. Since we are not aware of an exact mathematical connection, the Rényi entropy metric is compared with metrics based on finite Lyapunov exponents.

These originate from chaos theory and essentially tell how small line segments or uncertainties grow or shrink with time. Using the model as a test bench, we can make quantitative comparisons between the Rényi entropy and the Lyapunov exponents, to assess the validity of the former as a diagnostic for transport and mixing in the stratosphere. The main goal can be summarised in answering the following questions:

1. Is the Rényi entropy metric suitable as a diagnostic of stratospheric transport and mixing?

2. What conditions must then be fulfilled for the Rényi entropy metric to be useful?

3. What are the strengths and weaknesses with the metric compared to other metrics?

## 1.1 Purpose

At present, stratospheric chemistry models do not fully agree with observations (*SPARC Report No. 5*, 2010). These models are crucial in order to predict for example greenhouse gas distributions, the spreading of pollutants or the structure of the Antarctic ozone hole (Wallace and Hobbs, 2006). To improve model performance, good and well understood diagnostics of transport and mixing are valuable.

Most conventional metrics are based on calculating Lagrangian trajectories. This is typically computationally heavy, but foremost it is based on knowing the

velocity field of the flow. Measuring wind fields globally on Earth is however very difficult, and usually comes with large measurement uncertainties. Tracer fields are on the other hand easier to measure globally. Consequently a tracer based metric, like the Rényi entropy metric, would be valuable in the atmospheric context.

## 1.2 Limitations

This thesis should correspond to 30 ETCS credits, i.e. 20 weeks of full time studies. With the relatively short time frame in mind, some clear limitations of the project are important. To start with, we only consider the three metrics stated above; i.e. the Rényi entropy metric, the finite time Lyapunov exponents and the finite size Lyapunov exponents, although other metrics also do exists in the literature (e.g. the effective diffusivity by Nakamura (1996)). We restrict the analysis to flows typical for the stratosphere and let these be two dimensional and incompressible. The metrics are however general and could equally well be applied on other types of systems. We only consider scalar tracer fields and evenly spaced spatial grids. The focus of the thesis lies on the measurement of transport and mixing and little will therefore be said about the underlying mechanisms that give rise to the mixing. We further allow ourselves to choose numerical methods without full motivation.

## 1.3 Thesis outline

The thesis starts with a chapter on the background and theory that will be used to understand, implement and evaluate the metrics. First the dynamics of the stratosphere is briefly introduced. In particular, the main transport and mixing properties are covered. The Rényi entropy is thereafter introduced in a general sense followed by a review of the Lyapunov exponents. The theoretical, so called characteristic Lyapunov exponents are introduced and followed by their numerical realisations: the finite time and finite size Lyapunov exponents.

Based on the previous chapter, the methods are presented. First the simple stratospheric model is introduced, which tries to mimic the main dynamical features of the stratosphere covered in the previous chapter. The implementation of the Rényi entropy metric as an image filter of simulated tracer fields is then explained. The algorithms for computing the finite Lyapunov exponents are then presented.

Following the method chapter, the results are presented. Aspects as dependence on design parameters, ability to reflect particle transport and dependence on initial tracer fields for the Rényi entropy are considered. The results for the finite Lyapunov exponents are shown and a comparison between these and the

Rényi entropy is presented.

The thesis ends with a discussion of the results and the final conclusions are made.

# 2

# Background

## 2.1 The stratosphere

The atmosphere is usually described in terms of different layers, where each layer is defined by some characteristic physical or chemical properties. Most commonly they are defined by their vertical temperature gradient, in which case the atmosphere is splits into: the troposphere, stratosphere, mesosphere and thermosphere (see figure 2.1). In this thesis we turn our attention exclusively to the stratosphere and will only mention the other layers in relation to it.

As shown in figure 2.1, the stratosphere is defined by a steep positive temperature gradient, i.e. warmer air is on top of colder air. Since cold air typically is denser than warm air, this makes it very stable to vertical perturbations and thus stratified. In general terms, when we cannot assume constant pressure, the connection between temperature and density is made in terms of *potential temperature*:

$$\Theta = T\left(\frac{p}{p_0}\right)^{-\kappa} \tag{2.1}$$

where $T$ is temperature, $p$ is pressure and $\kappa$ is a constant. This is the temperature that a volume of air would have if brought adiabatically[1] to a reference pressure $p_0$. Thus, with respect to potential temperature we have vertical stability if $\partial\Theta/\partial z > 0$,

[1] In the atmosphere, this usually means that we assume no radiative absorption (or emission) or any phase changes of water in the volume of air.

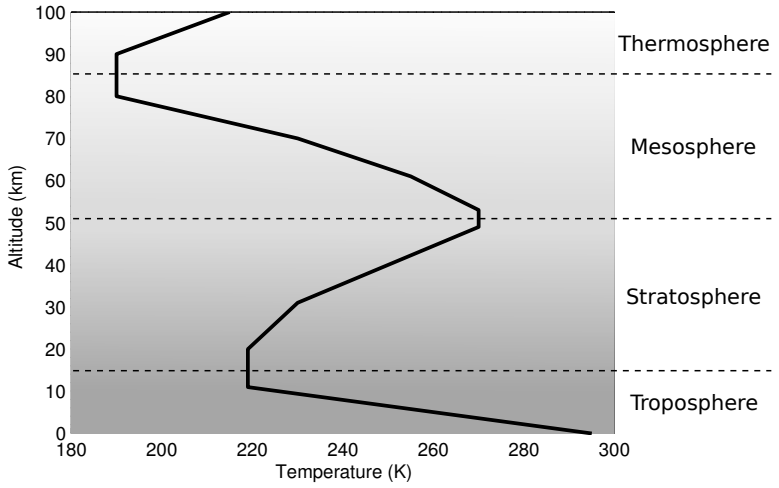


**Figure 2.1:** A characteristic vertical temperature profile of the atmosphere, with corresponding layers. The stratosphere is characterised by a positive temperature gradient.

which usually is the case in the stratosphere[2] (Haynes, 2005).

Potential temperature is not only useful in terms of identifying vertical stability. As it turns out, $\Theta$ typically increases monotonically with height in the stratosphere and therefore works as an alternative measure of height (Andrews et al., 1987, page 343). That is, positions can be written as $(x,y,\Theta(z))$, where $x$ is longitude, $y$ is latitude and $z$ is height. When studying transport and mixing this has the advantage that, adiabatic motion flows along surfaces of constant potential temperature, called *isentropic surfaces*, and thus becomes two dimensional, while diabatic motion flows across the surfaces and becomes one dimensional. Adiabatic transport and mixing is typically more rapid (Shepherd et al., 2000) and for our concerns we therefore assume the flows to be two dimensional.

### 2.1.1 Transport and mixing

Dynamical features of flows are commonly visualised by observing tracers that follow the flow. In laboratory experiments this is typically some dye that is added, while in the atmosphere it is often the concentration of some long lived chemical

[2]The connection between potential temperature gradients and temperature gradients (and figure 2.1) can further be shown to be $\partial\Theta/\partial z = T(\partial T/\partial z + \kappa g/R)$ (see e.g. Andrews et al. (1987), page 6), where $g$ is the gravitational acceleration and $R$ is the gas constant. Thus, in terms of temperature, $\partial T/\partial z > -\kappa g/R$, implies vertical stability.

substance. We can identify at least three processes that affects the distribution of tracers: *transport*, *mixing* and *diffusion*. With transport we simply mean the process of moving the tracer distribution away from its source. Mixing[3] we identify as the process of deforming the shape of the distribution by stretching and folding, often resulting in filaments. Diffusion is finally the motion on the molecular scale that acts to make the distribution smooth.

Formally these processes are described by the diffusion-advection equation:

$$\frac{\partial C}{\partial t} + \mathbf{u} \cdot \nabla C = D\nabla^2 C \tag{2.2}$$

where $C = C(\mathbf{x},t)$ is the tracer field, $\mathbf{u} = \mathbf{u}(\mathbf{x},t)$ is the velocity field and $D$ is molecular diffusivity. The first term on the left hand side represents sources and sinks in the tracer field and will for simplicity be neglected. The second term, where the velocity field enters, accounts for the advection and thus the transport and mixing, while the right hand side accounts for molecular diffusion. As it turns out, the advection term typically dominates the diffusion term in the stratosphere (Haynes, 2005, page 267) and we therefore ignore the latter. This further means that the tracer values stays constant as they follow their air parcel trajectories.

The starting point to the problem of describing transport and mixing is thus the specification of the velocity field $\mathbf{u}(\mathbf{x},t) = (u,v)$, with components $u = u(x,y,t)$ being longitudinal wind and $v = v(x,y,t)$ latitudinal wind. A precise description is then acquired by solving the velocity field and measuring by how much the tracer move, stretch and fold as they follow their trajectories. While this might sound straight forward in theory, even very simple velocity fields can produce very complicated trajectories, resulting in so called *chaotic advection*. A general and precise description is therefore typically difficult to achieve and with that in mind, we make qualitative assessments by comparing the different metrics instead of working from first principles.

### 2.1.2 A simple picture

A rough idea of what the typical transport and mixing properties of the stratosphere looks like can be made by identifying the following three regions (see figure 2.2): the *winter polar vortex*, the *surf zone* and the *tropical pipe*. During winter, a large vortex appears over the corresponding pole. The southern polar vortex is typically stronger and more coherent then the northern one, due to the larger areas of land on the northern hemisphere that give rise to perturbing gravity waves[4]. The edge of the winter polar vortex makes up a distinct barrier to pole-ward transport.

[3]What we call mixing is sometimes referred to as *stirring* instead.

[4]Gravity waves are not to be confused with gravitational waves in general relativity.

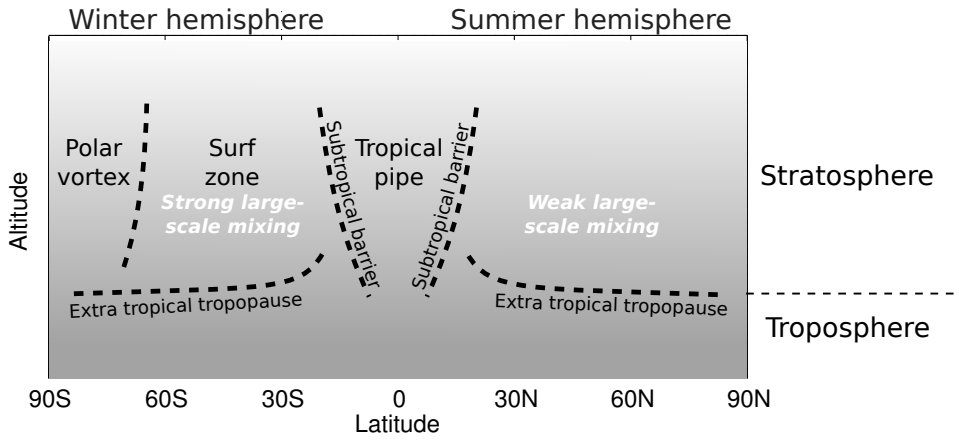


**Figure 2.2:** A schematic picture of the transport and mixing regions of the stratosphere. Transport barriers are shown as dotted lines. Bounded by the barriers, the dynamics is characterised by large scale advective mixing which is particularly strong in the surf zone. For a more extensive picture, see for example Haynes and Shuckburgh (2000).

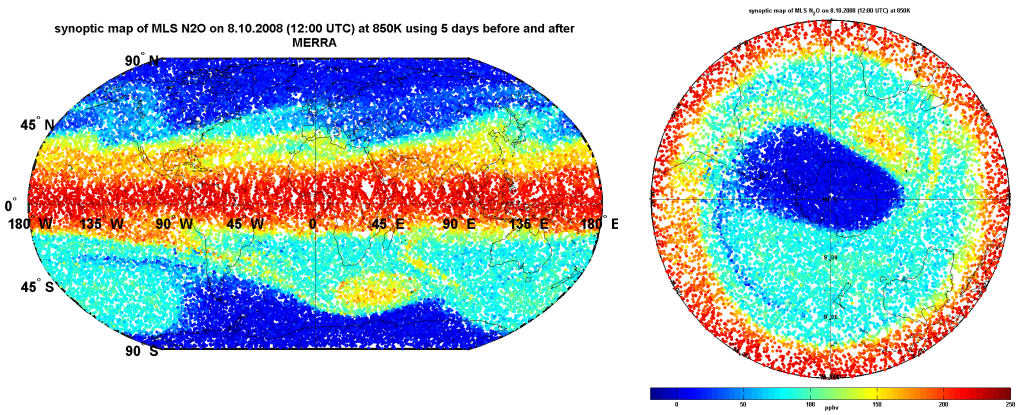


**Figure 2.3:** The distribution of the trace gas $N_2O$ in the stratosphere derived from data assimilation (EOS MLS and domain-filling) shows large scale advective features. (a) shows the tropical pipe with high concentrations over the equator and large planetary waves between the poles and subtropical barriers. (b) shows the southern polar vortex at winter. Images provided by Nikolai Krützmann.

The surf zone (Plumb, 1996) is the region between the winter polar vortex and the tropical pipe. It is characterised by large scale planetary waves that break (thus the term "surf zone"), forming large filaments in the tracer fields. The tropical pipe is a region of comparably large vertical transport and most chemical tracers from the troposphere enter the stratosphere via this region. Outside the tropical pipe, vertical transport is small and the *extra-tropical tropopause* can be identified as a transport barrier towards the troposphere. The edges of the tropical pipe can be identified as a barrier to equator-ward transport, called the *subtropical barriers*.

Satellite observations of long lived trace gases show some of these transport and mixing features, as depicted in figure 2.3. The three mixing regions can be identified by the strong gradients in chemical concentration reflecting the horizontal transport barriers between them and we also see large scale filaments in the mid latitudes representing the surf zone.

## 2.2 Rényi entropy

The *Rényi entropy* is a quantity that originates from information theory. It essentially gives a measure of the complexity of a discrete *probability distribution function* (PDF). The PDF is derived from some random variable, which in our case will be a tracer value. We denote the probability that this variable will take a discreet value $c_i$ as:

$$p_i = \text{"probability that } C = c_i\text{"} \tag{2.3}$$

where $i = 1,...,b$. We require that all probabilities must add up to one:

$$\sum_{i=1}^{b} p_i = 1 \tag{2.4}$$

The Rényi entropy is then defined as (Renyi, 1960):

$$H_\alpha = \frac{1}{1-\alpha} \ln \left( \sum_{i=1}^{b} p_i^\alpha \right) \tag{2.5}$$

where $\alpha$ is a parameter that takes integer values. The special case $\alpha = 1$ can be shown to reduce to the well known *Shannon entropy* (Renyi, 1960):

$$H_1 = -\sum_{i=1}^{b} p_i ln(p_i) \tag{2.6}$$

which can be interpreted as a measure of information (Shannon, 1948, page 11). In this thesis we follow Krützmann et al. (2008) and we restrict ourselves to the case $\alpha = 2$ only, which we will simply refer to as the Rényi entropy:

$$H_2 = -\ln\left(\sum_{i=1}^{b} p_i^2\right) \tag{2.7}$$

It can be shown that if all $c_i$ are equally probable, i.e. the PDF is homogeneous, the Rényi entropy is maximized and it follows from eq. 2.5 that this equals $\ln b$. Using this fact, we can normalise the entropy in order to make comparisons easier, and define the normalised Rényi entropy as:

$$\hat{H}_2 = -\frac{1}{\ln b}\ln\left(\sum_{i=1}^{b} p_i^2\right) \tag{2.8}$$

A homogeneous PDF thus yields unit Rényi entropy. If there is only one possible $c_i$ the Rényi entropy is zero.

The main assumption when using Rényi entropy as a measure of mixing is thus that the complexity of the discrete probability distribution of tracer values reflects the geometrical stretching and folding of the tracer field. Note that the entropy only depends on the probability distribution and not the values themselves, which is expected since the transport and mixing only alters the distribution of values.

## 2.3 Lyapunov exponents

The concept of Lyapunov exponents originates from dynamical systems theory as a diagnostic of chaos. They state how initially small perturbations or line segments grow or shrink with time. In terms of mixing, they can be seen to give the average stretching rates of material lines (Ottino, 1989). We distinguish between the theoretical, so called *characterstic Lyapunov exponents* (CLEs) and their numerical realisations: the *finite time Lyapunov exponents* (FTLEs) and the *finite size Lyapunov exponents* (FSLEs).

### 2.3.1 Characteristic Lyapunov exponents (CLEs)

The characteristic Lyapunov exponents specifies how infinitesimal line segments grow or shrink in the limit as time goes to infinity. Given some initial point $\mathbf{x}_0$, we perturb it slightly and define the corresponding initial line segment as $\delta\mathbf{x}_0 = \mathbf{x}_0 - \tilde{\mathbf{x}}_0$. We denote the line segment after some time $t$ as $\delta\mathbf{x}(t)$ and define

the CLE[5] as the logarithm of the rate of stretching per unit time (Ott, 2002):

$$\lambda(\mathbf{x}_0) = \lim_{t\to\infty} \lim_{|\delta\mathbf{x}_0|\to 0} \frac{1}{t} \ln\left(\frac{|\delta\mathbf{x}(t)|}{|\delta\mathbf{x}_0|}\right) \tag{2.9}$$

If the exponent is independent on the initial position $\mathbf{x}_0$ the system is called *ergodic* (Eckmann and Ruelle, 1985), while otherwise it is *non ergodic* and results in a time independent Eulerian field. In general the line segment can grow or shrink along any dimension of the system and there are thus for $n$ dimensional systems $n$ exponents, which we write $\lambda_i$, where $i = 1,...,n$. Each exponent is associated with a *specific* initial line segment $\delta\mathbf{x}_{0i}$. It is customary to order the set of all exponents from the largest to the smallest and form the so called *Lyapunov spectrum* as $\lambda_1 > \lambda_2 > ... > \lambda_n$. In our case, we simply have two exponents and for incompressible flows, the sum of exponents is zero:

$$\lambda_1 + \lambda_2 = 0 \tag{2.10}$$

This can be shown using the fact that the area spanned by the infinitesimal segments must be conserved for incompressible flows.

If one or more exponent is positive the system is said to be *chaotic*, since for long enough times we have roughly

$$|\delta\mathbf{x}(t)| \approx |\delta\mathbf{x}_0| \mathrm{e}^{\lambda_1 t} \tag{2.11}$$

That is, small line segments (or uncertainties) grow exponentially fast on average and the largest exponent dominate the growth[6].

An alternative way of writing the CLEs is to make use of the so called *variational equation*, which govern the time evolution of infinitesimal line segments. It can be found by linearisation of the velocity field and will be useful when defining the finite time Lyapunov exponents. Taylor expansion of the wind field $\mathbf{u}(\mathbf{x},t)$ around the perturbed point $\tilde{\mathbf{x}}$ yields:

$$\mathbf{u}(\mathbf{x}+\delta\mathbf{x},t) = \mathbf{u}(\mathbf{x},t) + \mathbf{J}\delta\mathbf{x} + \mathcal{O}(|\delta\mathbf{x}|^2) \tag{2.12}$$

where $\mathbf{J}$ is the *Jacobian matrix*, i.e. the spatial derivatives of $\mathbf{u}(\mathbf{x},t)$:

$$\mathbf{J} = \begin{bmatrix} \frac{\partial u}{\partial x} & \frac{\partial v}{\partial x} \\ \frac{\partial u}{\partial y} & \frac{\partial v}{\partial y} \end{bmatrix} \tag{2.13}$$

[5]The existence of the CLE is guaranteed by *Oseledets multiplicative theorem* (Oseledets, 1968).

[6]The inverse of the largest exponent is sometimes used as a measure of the time scale for which certainty can be assumed (Boffetta et al., 2001).

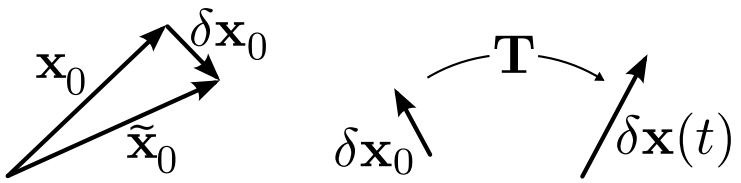


(a) Line segment. (b) Tangent matrix.

**Figure 2.4:** (a) illustrates a small line segment. It get mapped from its initial time to a future time $t$ by the tangent matrix $\mathbf{T}$ as illustrated in (b).

If we let the line segment be sufficiently small, higher order terms in eq. 2.12 can be neglected. Using the simple fact that $\mathbf{u} = \mathrm{d}\mathbf{x}/\mathrm{d}t$ we further get:

$$\frac{\mathrm{d}\delta\mathbf{x}}{\mathrm{d}t} = \mathbf{J}\delta\mathbf{x} \tag{2.14}$$

We now have a differential equation that governs the evolution of an infinitessmial segment. We further make the following ansatz:

$$\delta\mathbf{x}(t) = \mathbf{T}(t)\delta\mathbf{x}_0 \tag{2.15}$$

That is, we assume $\delta\mathbf{x}_0$ is mapped to future times linearly by the matrix $\mathbf{T}$, called the *tangent matrix*. If we plug this into eq. 2.14, we can rewrite it in terms of the tangent matrix:

$$\frac{\mathrm{d}\mathbf{T}}{\mathrm{d}t} = \mathbf{J}\mathbf{T} \tag{2.16}$$

This is called the variational equation. All information about the stretching of the initial line segments and hence the mixing is contained in the tangent matrix. The stretching can be made explicit by QR factorisation, for which we write $\mathbf{T}$ as the product of a orthonormal matrix[7] $\mathbf{Q}$ and a right triangular matrix $\mathbf{R}$, such that:

$$\begin{bmatrix} T_{11} & T_{12} \\ T_{21} & T_{22} \end{bmatrix} = \begin{bmatrix} Q_{11} & Q_{12} \\ Q_{21} & Q_{22} \end{bmatrix} \begin{bmatrix} R_{11} & R_{12} \\ 0 & R_{22} \end{bmatrix} \tag{2.17}$$

The elements of $\mathbf{R}$ contains the stretching and skewing of the orthonormal column vectors of $\mathbf{Q}$ in order to produce $\mathbf{T}$ as shown in figure 2.5. In particular the diagonal elements $R_{11}$ and $R_{22}$ specifies the stretching and the off diagonal element $R_{12}$ specifies the skewing. The CLEs can now be written in terms of the diagonal

[7]Orthonormal essentially means that the column vectors are orthonormal vectors to each other.

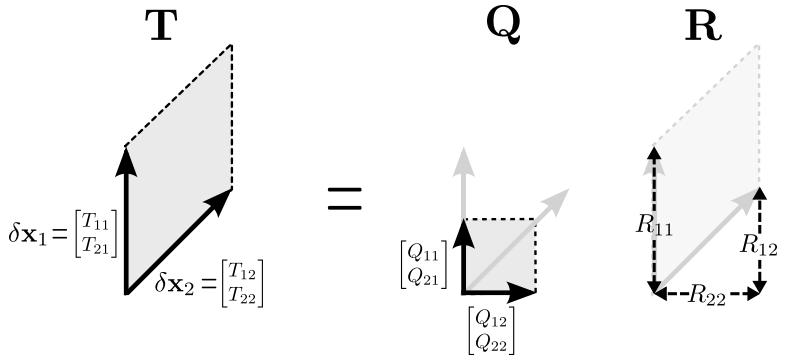


**Figure 2.5:** Illustration of the QR factorisation of the tangent matrix.

elements as[8] (see Appendix A and further for example Eckmann and Ruelle (1985); Geist et al. (1990)):

$$\lambda_i(\mathbf{x}_0) = \lim_{t\to\infty} \frac{1}{t} \ln\left(|R_{ii}|\right) \tag{2.18}$$

### 2.3.2 Finite time Lyapunov exponents (FTLEs)

While the CLEs are defined as time goes to infinity, we are concerned with mixing over finite times. The appropriate measure is then the finite time Lyapunov exponents, which we define as:

$$\lambda_i^t(\mathbf{x}_0) = \frac{1}{t} \ln\left(|R_{ii}|\right) \tag{2.19}$$

where $t$ is now a finite time. Here we make use of eq. 2.18 to make the limit as the initial line segment goes to zero implicit.

### 2.3.3 Finite size Lyapunov exponents (FSLEs)

While the limit as the line segment goes to zero is made implicit for the FTLE by introducing the variational equation (eq. 2.16), this relies on knowing the Jacobian of the flow. In many situations it is however not practical or possible to compute the Jacobian matrix analytically, for example when the velocity field is derived from observational data. One way of dealing with such situations is simply to use

[8]Yet another way of expressing the Lyapunov exponent is in terms of the eigenvalues of the tangent matrix (Pierrehumbert and Yang, 1992).

finite line segments. This yields the *finite size Lyapunov exponent* (Aurell et al., 1997; Boffetta et al., 2001), which we define as:

$$\lambda^{t,\Delta\mathbf{x}_0}(\mathbf{x}_0) = \frac{1}{t} \ln \left( \frac{|\Delta\mathbf{x}(t)|}{|\Delta\mathbf{x}_0|} \right) \tag{2.20}$$

where $\Delta\mathbf{x}_0$ is a *finite* initial line segment such that $\Delta\mathbf{x}_0 = \mathbf{x}_0 - \tilde{\mathbf{x}}_0$ and $\Delta\mathbf{x}(t) = \mathbf{x}(t) - \tilde{\mathbf{x}}(t)$.

It is worth mentioning that, while we distinguish the FSLE from FTLE as two different quantities, both are sometimes referred to as FTLE in the literature (for example Garny et al. (2007)). However, in this thesis we use the term FTLE exclusively for the method described in the previous section based on linearised equations.

# 3

# Method

## 3.1 A simple stratosphere

In order to simulate transport and mixing typical for the stratosphere, we adopt a model that roughly imitates the features noted in section 2.1.2. For this we find a previously studied family of flows suitable. These have been used in a similar context by Shuckburgh and Haynes (2003). Analytically the flows can be written in terms of a stream function[1]:

$$\Psi(x,y,t) = a\sin x - b\sin^3 x + c(y,t)\cos^3 x \tag{3.1}$$

where:

$$c(y,t) \equiv \epsilon_1 \cos y + \epsilon_2 \cos(y + \omega t)$$

Specified as a stream function, the requirement of incompressibility is fulfilled (Boffetta et al., 2001). The corresponding velocity field is then given as:

$$u = \frac{\partial \Psi}{\partial y}, \qquad v = -\frac{\partial \Psi}{\partial x} \tag{3.2}$$

defined by the five parameters $a$, $b$, $\epsilon_1$, $\epsilon_2$ and $\omega$. The first three; $a$, $b$ and $\epsilon_1$, determines the general structure of the field. The other two specifies the time dependent part which makes motion chaotic. By choosing appropriate values we can make a crude imitation of the typical stratospheric dynamics. By choosing $a = 0.25$, $b = 0.05$ and $\epsilon_1 = 0.25$, the flow yields two vortex structures surrounded by a jet, as shown by an arrow plot in figure 3.1(a). Note that if $\epsilon_2 = 0$ the

[1]The stream function is formally the Hamiltonian of the system.

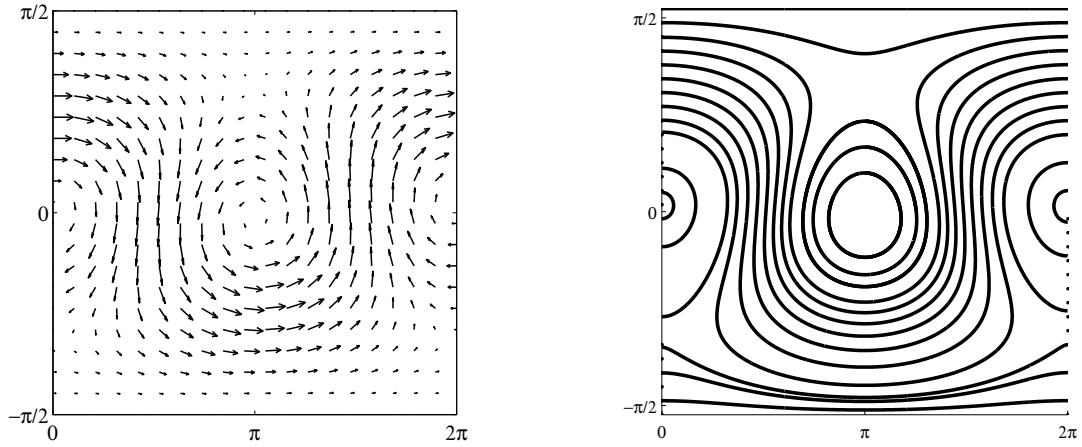


(a) (b)

**Figure 3.1:** (a) shows the velocity field as an arrow plot for the case $a = 0.25$, $b = 0.05$, $\epsilon_1 = 0.25$ at time $t = 0$. We see two vortex structures surrounded by a jet. If $\epsilon_2$ is non zero, the arrows will oscillate with frequency $\omega/2\pi$, which makes the flow chaotic. (b) shows the corresponding stream lines of the velocity field. For $\epsilon_2 = 0$ trajectories will follow the stream lines.

term in the stream function that contains time disappears. Trajectories are then integrable and the flow is laminar, as shown by the stream lines in figure 3.1(b). For non zero $\epsilon_2$, small perturbations with frequency $\omega/2\pi$ are introduced which, as we will see, give rise to filaments that roughly imitates planetary wave breaking in the surf zone.

### 3.1.1 Simulating tracer fields

Since the Rényi entropy depends on tracer fields, we must simulate these given the velocity fields of eq. 3.2. Since we have neglected molecular diffusion as well as sources and sinks the tracer values follow the trajectories passively. Thus, we simply solve the velocity field for a grid of initial positions, each associated with a tracer value, and define the tracer field as the tracer values at the final positions. To make sure that the tracer field becomes uniformly distributed in space, we want the final positions to end up on an evenly spaced grid. This can be achieved by integrating the trajectories backwards. That is, we solve the velocity field from the final time, say $t_1$, with corresponding evenly spaced positions $\mathbf{x}(t_1)$, to the initial time, say $t_0$, and corresponding positions $\mathbf{x}(t_0)$. We then map each initial position $\mathbf{x}(t_0)$ to a tracer value and associate it to the position $\mathbf{x}(t_1)$, as illustrated in figure

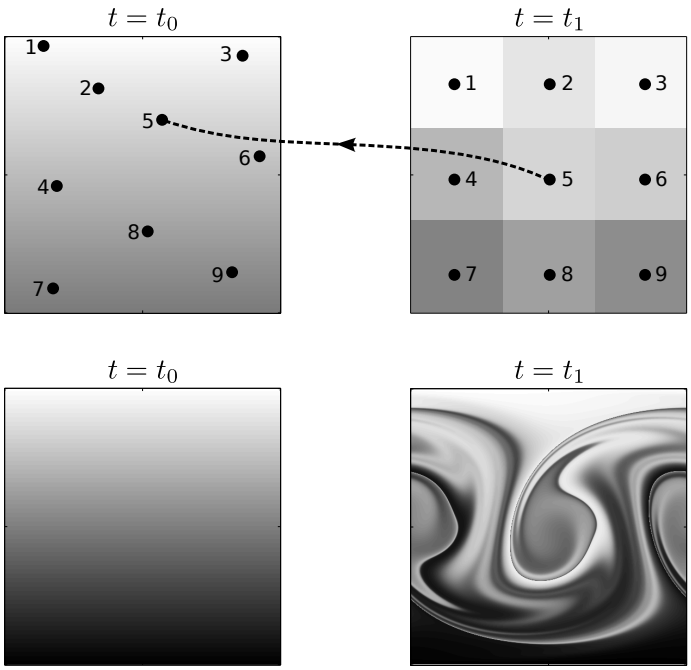


**Figure 3.2:** A schematic illustration of how a the tracer field is mapped from the initial time $t_0$ to the final time $t_1$ by backwards trajectories.

3.2.

For the numerical integration of the trajectories, an adaptive Runge Kutta algorithm has been used, specifically the MATLAB function ode45. It is based on the Dormand-Prince method, which is an explicit Runge-Kutta method with adaptive step size. In short, it computes both a fourth and fifth order Runge-Kutta step, estimates the error and adjust the step size according to a user defined error tolerance. We find the adaptive step size desirable since the flow may show fractal structures in the chaotic regime, i.e. fluid filaments may appear on multiple scales. Since the trajectories in the grid do not depend on each other, this further give us the opportunity to integrate the grid of initial positions in parallel, using the Matlab Parallel Computing Toolbox.

## 3.2 Implementation of Rényi entropy

The Rényi entropy metric is essentially implemented as an image fitler, as illustrated in figure 3.3. In particular we consider a quadratic filter region of values on which the Rényi entropy is calculated. The probability distribution is created by placing the tracer values into $b$ number of bins, each representing a small range of

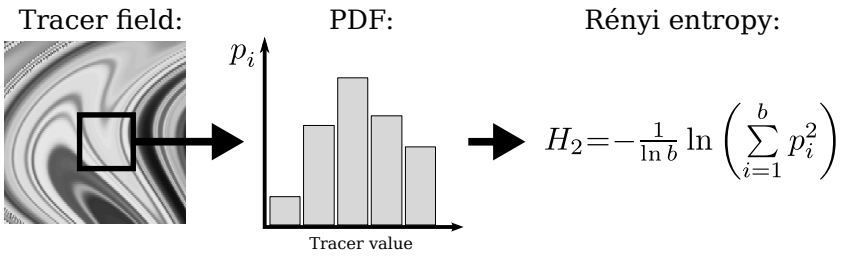


**Figure 3.3:** The tracer field is filtered with a quadratic filter region. The tracer values in the region are used to construct a discrete probability distribution on which the Rényi entropy is calculated.

tracer values. We force bins to cover the range of all values in the global tracer field. We thus get a localised distribution but with bins that references values corresponding to the global tracer field. The probability distribution is thus:

$$p_i = \frac{n_i}{\sum_{i=1}^{b} n_i} \tag{3.3}$$

where $n_i$ is the number of tracer values that corresponds to bin labelled by the integer $i$. The normalised Rényi entropy is then calculated according to eq. 2.8.

### 3.2.1 Design parameters

We may here identify three parameters that we must choose for the Rényi entropy metric: the number of bins to be used in the constructed probability distributions, the filter size (i.e. the number of grid points contained in the filter window) and the grid resolution. The number of bins can be interpreted as the number of material lines or tracer contours considered in the tracer field, as illustrated in figure 3.4. The act of discretising the tracer values in bins is due to result in a loss of information and structure in the tracer field. In that respect it is desirable to have a high number of bins.

At the same time, the number of bins must be chosen such that a meaningful probability distribution can be constructed. If the bins are too many, the distribution will loose its shape and fail to represent the complexity of the tracer values. This can be illustrated by generating two sets of random numbers according to two different probability distributions: one made up of two displaced Gaussian peaks and the other a flat distribution. We plot the Rényi entropy for the two sets of random numbers for different number of bins, as shown in figure 3.5. It shows that as the number of bins grow very large, the entropy for the two sets goes towards

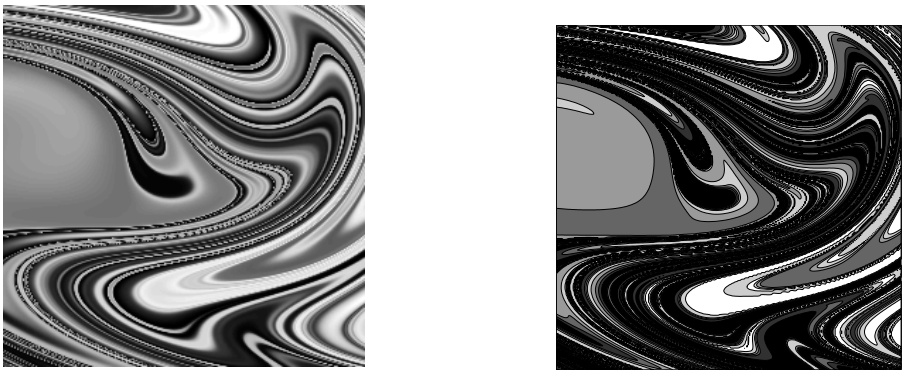

(a) (b)

**Figure 3.4:** By binning the continuous tracer field in (a), we essentially define material lines as in (b). This particular case would correspond to 5 bins.

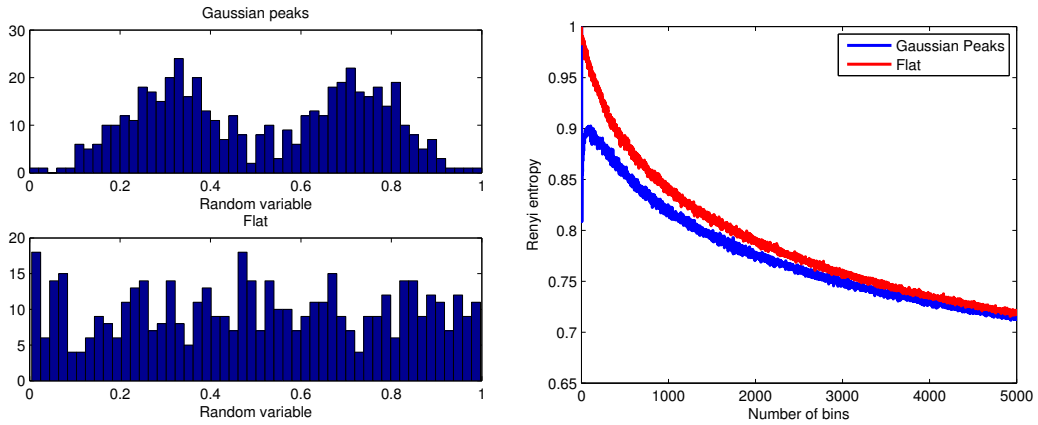


(a) (b)

**Figure 3.5:** 500 random point are generated according to two different probability distributions as seen to the left. The Rényi entropy is plotted for different number of bins to the right, illustrating that too many bins make the Rényi entropy essentially the same for both distributions.

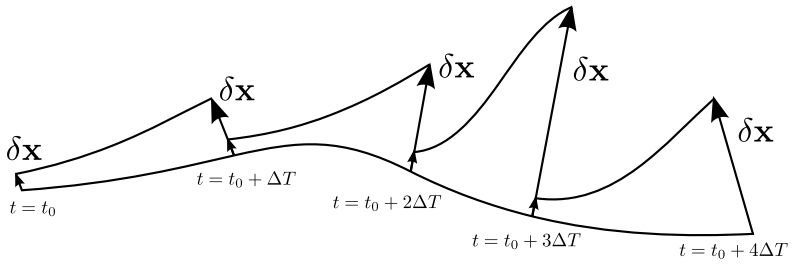


**Figure 3.6:** Periodical re-normalisation of the displacement between two trajectories is invoked to avoid numerical overflow.

the same value, although the underlying distributions are very different. One way of choosing the bin number is to use a so called optimal binning algorithm (Krützmann et al., 2008). The algorithm, which was provided by Nikolai Krützmann, analyses the tracer values to find the optimal number of bins in order to estimate the distribution.

The grid resolution sets a limit on the smallest scale of filaments that can be resolved. The filter size must further be small enough to make the metric localised, but big enough to cover the filaments.

## 3.3 Implemetation of Lyapunov exponents

Regardless if we want to implement the FTLE or the FSLE we face an immediate numerical problems if one or more exponent turn out to be positive. The first is that after sufficiently long times, the line segments will grow exponentially in the direction of the largest exponent which eventually leads to numerical overflow (see eq. 2.11). To avoid this, it is useful to normalise the length of the line segments. Normalisation can be invoked periodically (Garny et al., 2007) or when the segments grows larger than some specified threshold (Boffetta et al., 2001; Shuckburgh and Haynes, 2003). For the FSLE we choose to do this periodically with period $\Delta T$, at times $t = t_0 + k\Delta T$, where $k = 0,...,m-1$ and $m = (t_1 - t_0)/m$. For the FTLE we normalise if the segments grows larger than a factor $r$, but we check this at the same normalisation times as for the FSLE.

Another numerical problem is that if one exponent is positive, the growth in the corresponding direction will dominate. Any line segment with a component in that direction will align to it after sufficiently long time (which is short if the exponent is large). In other words, almost all the initial line segments will tend to align with the direction of largest growth. If we want to evaluate only the largest exponent, this is not a problem. If we want to calculate more than one

exponent, we need to re-align the line segments as well as to re-normalise their lengths (Wolf et al., 1985). In this thesis we are only interested in the maximal exponent and thus re-alignment is not needed. For the FTLE which we have expressed by QR factorisation, we get the normalised line segments for free in terms of the orthonormal column vectors of $\mathbf{Q}$ (Geist et al., 1990) (see figure 2.5). For the FSLE on the other hand, we make no re-alignments.

### 3.3.1 The FTLE algorithm

The FTLE we calculate as the average exponent over all normalisations periods:

$$\lambda_i^{(t_1-t_0)}(\mathbf{x}_0) = \frac{1}{t_1 - t_0} \sum_{k=0}^{m-1} \ln\left(|R_{ii}(k)|\right) \tag{3.4}$$

An advantage with expressing the FTLE in terms of $\mathbf{R}$ is that the corresponding $\mathbf{Q}$ contains the appropriate re-aligned initial line segments for the next normalisation period. We can describe the algorithm for the FTLE as follows (Eckmann and Ruelle, 1985; Geist et al., 1990; Wolf et al., 1985):

1. Let $\mathbf{x}(0) = \mathbf{x}_0$ and $\mathbf{T}(0) = \mathbf{I}$.
2. For each time specified by $k = 0,...,m-1$:
   (a) Solve the velocity field with initial condition $\mathbf{x}(k)$ and simultaneously the variational equation (eq. 2.16) with initial condition $\mathbf{T}(k)$ to get $\mathbf{T}(k+1)$.
   (b) QR factorise[2] $\mathbf{T}(k+1) = \mathbf{QR}$.
   (c) Extract the diagonal of $\mathbf{R}$ and add to a sum $S_i := S_i + \ln\left(|R_{ii}|\right)$.
   (d) If $|R_{ii}(k)|$ is larger than some threshold $r$, let $\mathbf{T}(k+1) = \mathbf{Q}$.
3. Calculate $\lambda_i^{(t_1-t_0)}(\mathbf{x}_0) = S_i/(t_1 - t_0)$
4. Take the maximal exponent.

Note that the variational equation depends on velocity (in the Jacobian) and thus both the velocity field and the variational equation are solved for simultaneously. The trajectories acquired form the velocity field can further be used when simulating tracer fields as described in section 3.1.1.

[2]There are different numerical methods for doing this. Studies like Eckmann and Ruelle (1985) suggests using the so called Householder transform, however we rely on Matlab to be implemented in a numerically suitable way.

### 3.3.2 The FSLE algorithm

Also the FSLE we calculate as the average exponent over all normalisations as:

$$\lambda^{(t_1-t_0),\Delta\mathbf{x}_0}(\mathbf{x}_0) = \frac{1}{t_1 - t_0} \sum_{k=0}^{m-1} \ln\left(\frac{|\Delta\mathbf{x}(k+1)|}{|\Delta\mathbf{x}_k|}\right) \tag{3.5}$$

The corresponding algorithm for the maximal exponent in two dimensions is as follows (Garny et al., 2007):

1. Let $\Delta\mathbf{x}(0) = [\begin{smallmatrix} d \\ 0 \end{smallmatrix}]$, where $d$ is a small number.
2. Let $\mathbf{x}(0) = \mathbf{x}_0$ and $\tilde{\mathbf{x}}(0) = \mathbf{x}(0) + \Delta\mathbf{x}(0)$.
3. For each time specified by $k = 0,...,m-1$:
   (a) Solve the velocity field for the two initial conditions $\mathbf{x}(k)$ and $\tilde{\mathbf{x}}(k)$ to get $\mathbf{x}(k+1)$ and $\tilde{\mathbf{x}}(k+1)$.
   (b) Let $\Delta\mathbf{x}(k+1) = \mathbf{x}(k+1) - \tilde{\mathbf{x}}(k+1)$
   (c) Add to sum $S := S + \ln(|\Delta\mathbf{x}(k+1)|/|\Delta\mathbf{x}(k)|)$
   (d) Normalise the segment $\Delta\mathbf{x}(k+1) := \Delta\mathbf{x}(k+1)/|\Delta\mathbf{x}(k+1)|$
4. Calculate $\lambda^{(t_1-t_0),\Delta\mathbf{x}_0} = S/(t_1 - t_0)$
5. Repeat step 2-4 with $\Delta\mathbf{x}(0) = [\begin{smallmatrix} 0 \\ d \end{smallmatrix}]$ and get $\lambda_2$
6. Take the maximal exponent.

Note also here, as for the FTLE, that the velocity field is solved for and thus the acquired trajectories can be used for simulating tracer fields as well.

# 4

# Results

## 4.1 Tracer field simulations

To start with, we consider a grid of 512x1024 grid points in latitude and longitude respectively and we let the initial time of integration be zero, i.e. $t_0 = 0$. For all numerical integrations we set the relative error tolerance between the integration steps to $10^{-6}$. These settings will be used in the rest of the thesis.

We note that both the FTLE and the FSLE solve for the velocity field when calculated and thus yields the trajectories from which the tracer fields can be constructed. These tracer fields are then to be used for the Rényi entropy metric, but also serves as a good way of visualising the flow. As an example we plot the evolution of an linear initially tracer field $C_0(x,y)$, such that $C_0(x,y) \equiv C(x,y,t_0) = y$, with the model parameters $(a, b, \epsilon_1, \epsilon_2, \omega) = (0.25, 0.05, 0.25, 0.1, 1)$, as shown

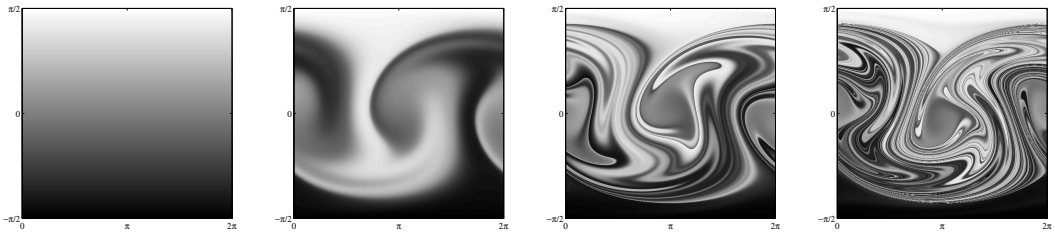

(a) $t_1 = 0$ (b) $t_1 = 3\tau$ (c) $t_1 = 6\tau$ (d) $t_1 = 9\tau$

**Figure 4.1:** Time evolution of a linear tracer field for the case $\epsilon_2 = 0.1$, where $\tau = 2\pi/\omega$.

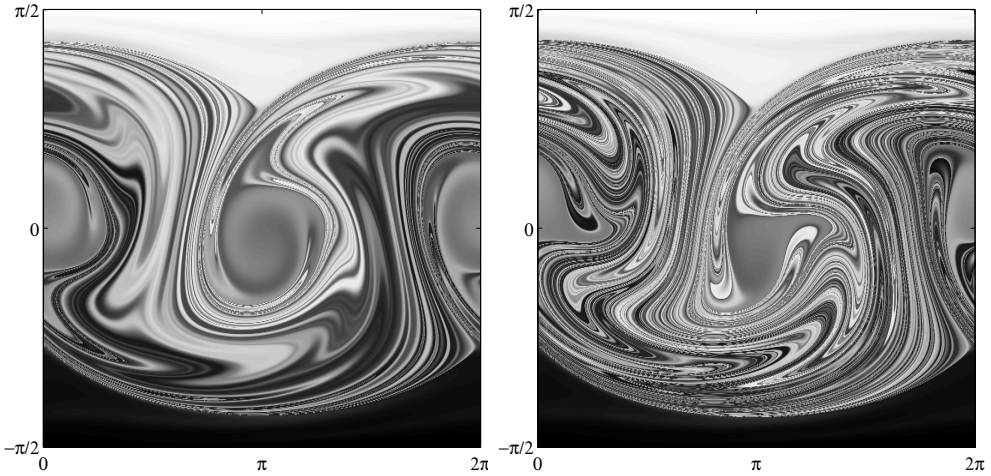


(a) $\epsilon_2 = 0.05$ (b) $\epsilon_2 = 0.15$

**Figure 4.2:** Two initially linear tracer fields are advected to time $t = 10\tau$, but for two different values of $\epsilon_2$. Higher value makes the flow more non linear and consequently the tracer field more mixed.

in figure 4.1. We can see how a jet zone with significant stretching and folding surrounds two vortex structures. This roughly imitates the transport and mixing features of the stratosphere, with a well mixed surf zone containing large scale filaments separated from the less mixed polar and tropical zones.

Recall that $\epsilon_2$ is a control parameter that makes the flow chaotic, which can be used as a mixing parameter. Higher $\epsilon_2$ means finer scaled filaments in the jet zone, as seen in figure 4.2. In the following we will use $(a, b, \epsilon_1, \omega) = (0.25, 0.05, 0.25, 1)$ unless stated otherwise and vary $\epsilon_2$ and the integration time $t_1$ to control the strength of mixing.

## 4.2 Rényi entropy

By generating tracer fields, considering $C_0(x,y) = y$, $t_1 = 10\tau$ and $\epsilon_2 = 0.1$, we now calculate the corresponding Rényi entropy fields. We choose 10 bins and the two filter sizes 9x9 and 25x25 grid points. The resulting entropy fields can be seen in figure 4.3. We identify that larger filter sizes makes the field smoother. In this particular case, it is further found that, using the optimal binning algorithm for choosing the number of bins has no major effect in the resulting Rényi entropy fields. It is however computationally much slower and we therefore restrict the bin number to 10 in the following, unless otherwise is specified.

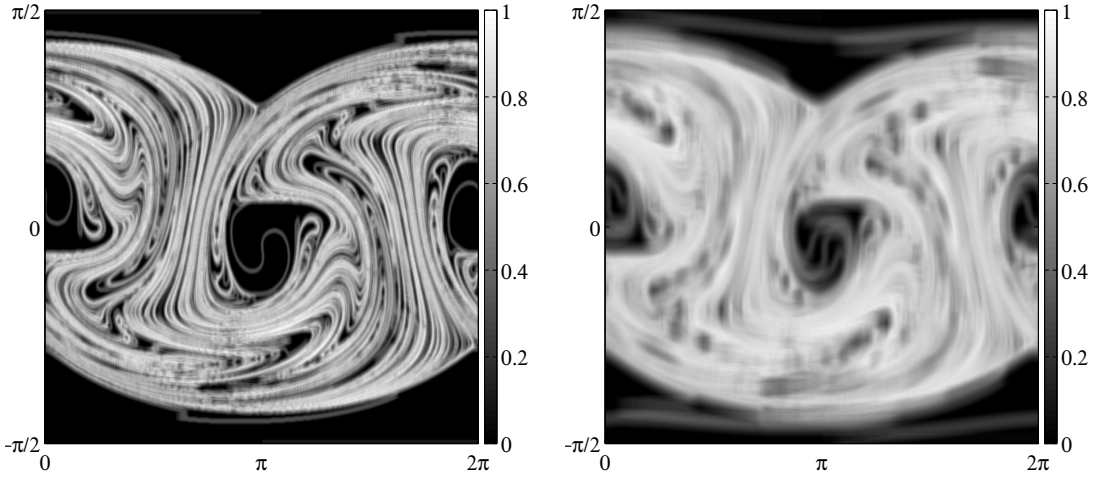


(a) RE 9x9 (b) RE 25x25

**Figure 4.3:** Rényi entropy fields generated from tracer fields, for the case $\epsilon_2 = 0.1$ and $t_1 = 10\tau$. Here 10 bins are used and the filter sizes 9x9 in (a) and 25x25 (b).

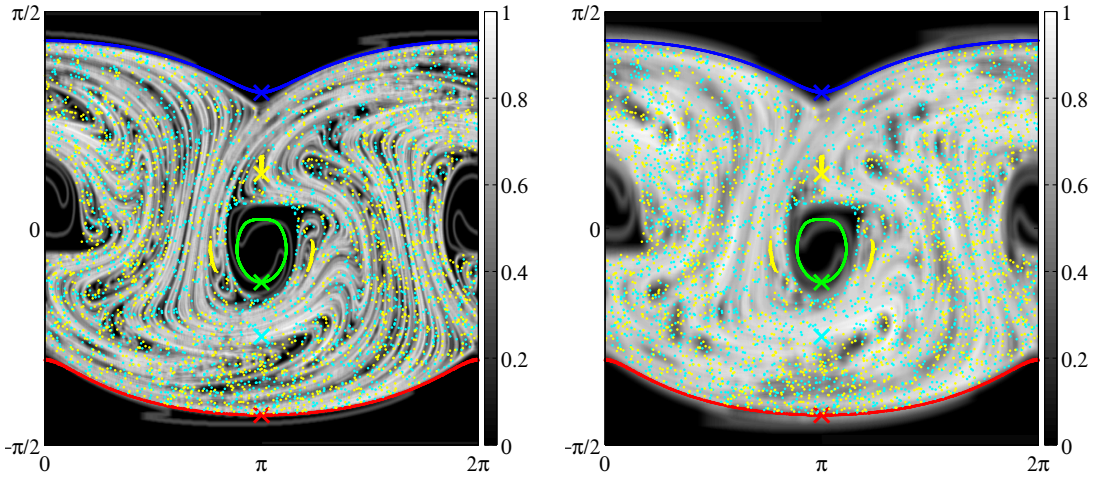


(a) RE 9x9 (b) RE 25x25

**Figure 4.4:** The Rényi entropy fields of figure 4.3 above with five overlayed Poincaré sections of different colours. The initial positions of the Poincaré sections are marked with crosses.

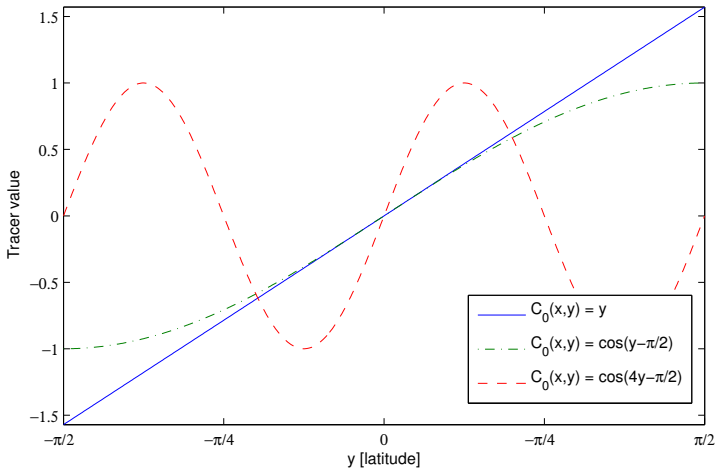


**Figure 4.5:** Vertical cross sections of the three different initial tracer fields considered.

### 4.2.1 Comparison to Poincaré sections

The ability to reflect particle transport can be analysed by comparison to so called *Poincaré sections* (Shuckburgh and Haynes, 2003). These are produced by integrating points over a very long time, here using $t_1 = 2500\tau$, and plotting them periodically. Doing this for five different initial positions and overlaying the resulting Poincaré sections on top of the previously considered Rényi entropy field, we get figure 4.4. Lines in the Poincaré sections indicates strong transport barriers while scattered dots indicates weak or no barriers. Here the Poincaré sections coloured in blue, green and red thus indicate strong transport barriers, the yellow indicates weaker barriers and the turquoise no barriers.

### 4.2.2 Changing initial tracer field

So far, we have considered a linear initial tracer field only, that is $C_0(x,y) = y$. Now we also consider the fields $C_0(x,y) = \cos(y - \pi/2)$ and $C_0(x,y) = \cos(4y - \pi/2)$, as shown in figure 4.5. In contrast to the linear tracer field, these fields have an initially inhomogeneous Rényi entropy. After advection, the entropy fields using a 9x9 filter are shown in figures 4.6(a)-(c). To see the effect of changing from the linear initial tracer field, we calculate the absolute differences as shown in figures 4.6(d)-(e). It is clear that changing from the linear field to $C_0(x,y) = \cos(4y - \pi/2)$ yields a larger difference in resulting entropy than changing to $C_0(x,y) = \cos(y - \pi/2)$.

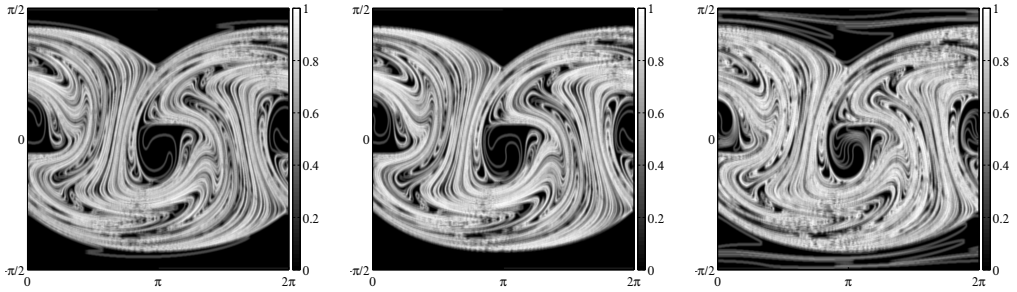


(a) Rényi entropy from $C_0 = y$

(b) Rényi entropy from $C_0 = \cos(y - \pi/2)$

(c) Rényi entropy from $C_0 = \cos(4y - \pi/2)$

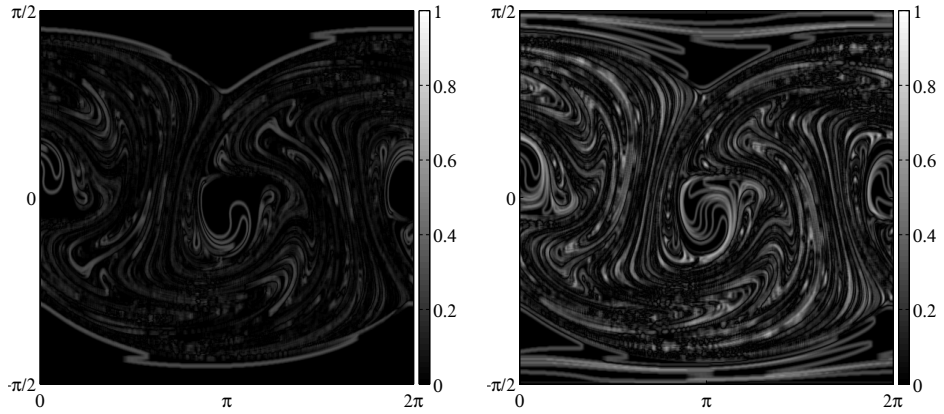


(d) Difference in RE: |(a) - (b)|

(e) Difference in RE: |(a) - (c)|

**Figure 4.6:** By advecting the three initial tracer field of figure 4.5, and generating Rényi entropy fields we get (a), (b) and (c). The absolute difference between (a) and (b) is shown in (d) and between (a) and (c) is shown in (e). We thus see that a change in the initial tracer field yield a change in the Rényi entropy field.

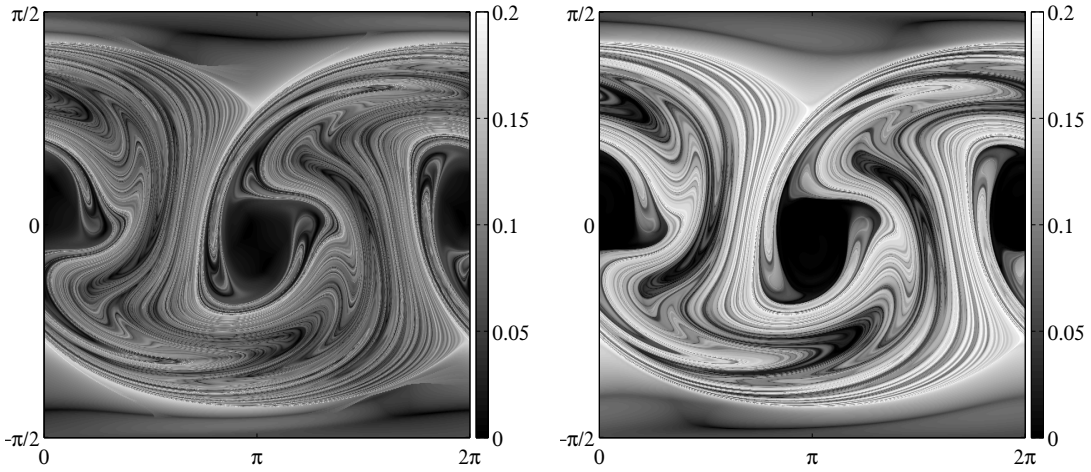


(a) FTLE (b) FSLE

**Figure 4.7:** (a) shows the FTLE field and (b) the FSLE field for the case $\epsilon_2 = 0.1$.

## 4.3 FTLE and FSLE

In order to further analyse the Rényi entropy metric, corresponding FTLE and FSLE fields are produced. For the FTLE we choose to invoke re-normalisation if the line segments grows by a factor $r = 10^3$. Using $t_1 = 10\tau$ and $\epsilon_2 = 0.1$ as for the Rényi entropy fields, we get the FTLE field shown in figure 4.7(a). For the FSLE we use an initial line segment equal to the displacement between the grid points (in this setting that means $|\Delta \mathbf{x}_0| = \pi/512$) and invoke re-normalisation periodically at times $t = k\tau/2$, where $k$ = 1,...,20. The corresponding FSLE field is shown in figure 4.7(b).

In the limit as the initial lines segment of the FSLE goes to zero and the number of re-normalizations goes to infinity, the two fields should in principle be the same. Here the FSLE field tends to give higher values as well as smoother features compared to the FTLE. In particular, sharp edges appears in the FTLE field in the less mixed upper and lower regions, which is not seen in the FSLE field. This might suggest that there is a numerical problem with the FTLE algorithm. It is however assumed to be of minor importance when using the FTLE for comparison to the Rényi entropy metric.

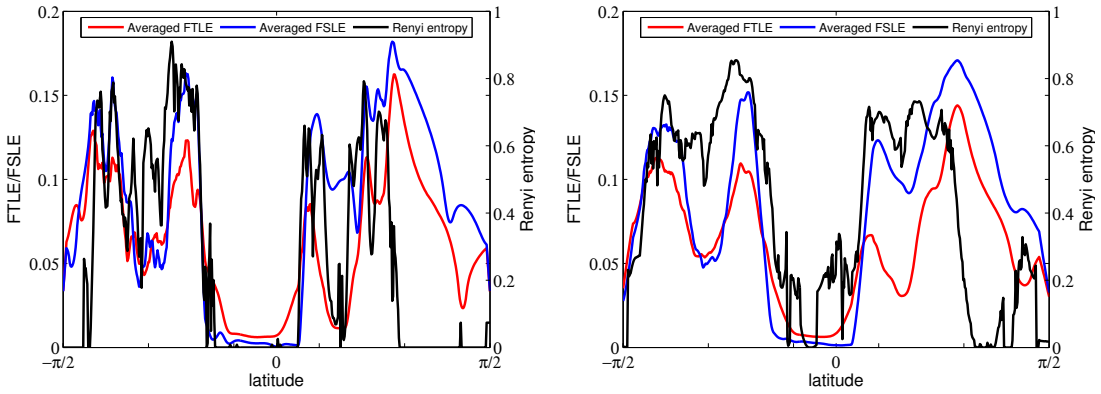


(a) RE, FTLE, FSLE: 9x9 filter

(b) RE, FTLE, FSLE: 25x25 filter

**Figure 4.8:** Cross-sectional plots of the FTLE, FSLE and Rényi entropy along the line $x = \pi$, for the two filter sizes 9x9 and 25x25. The Lyapunov exponents are averaged with the corresponding filter sizes and 10 bins are used for the Rényi entropy.

## 4.4 Correlations

We are now in position to compare the Rényi entropy fields to the finite Lyapunov exponent fields. Since the entropy metric depends on the filter size, we apply an averaging filter on the FTLE and FSLE fields, with the same filter size as used for the Rényi entropy. As a first comparison, we consider the case $\epsilon_2 = 0.1$ and plot the cross-sections of the fields along the line $x = \pi$ as seen in figure 4.8. The Rényi entropy appears to compare well in the jet zones. It however deviates at high latitudes for both filter sizes and in the vortex for the 25x25 filter size.

We can further analyse the correlation between the fields by scatter plots as shown in figure 4.9. Since plotting all the grid points makes the figures rather unclear, we have randomly picked out a sample of 3000 points (points closer than half the filter size from the boundaries are ignored to avoid effects of padding). It seems to indicate a somewhat linear relation, with a wider spread at low Rényi entropy values. The correlations are made explicit by computing linear correlation coefficients and Spearman correlation coefficients. The former, which assumes a linear relation varies between 0.43 and 0.53. The latter, which assumes a monotonic relation varies between 0.38 and 0.53.

Using the 9x9 filter, the coefficients are further examined by plotting the correlation coefficients versus $\epsilon_2$ and $t_1$ we get figure 4.10. It shows that both coefficients stays fairly constant with respect to $\epsilon_2$, with a high at $\epsilon_2 = 0.05$. For $t_1$, the coefficients increases until about $t_1 = 6\tau$ where they level out.

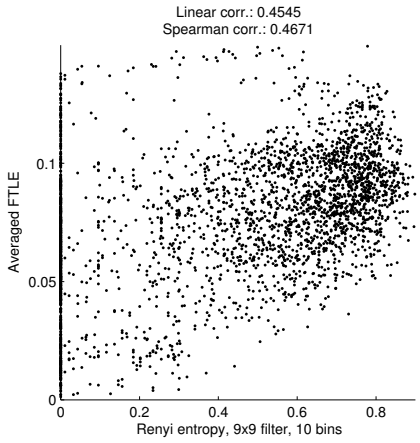


(a) RE vs. FTLE. 9x9 filter.

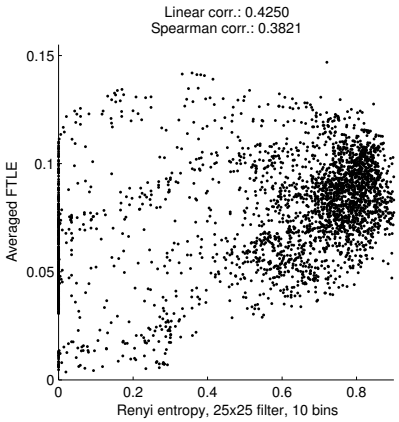


(b) RE vs. FTLE. 25x25 filter.

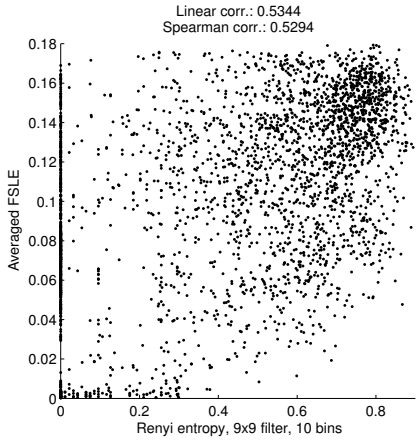


(c) RE vs. FSLE. 9x9 filter.

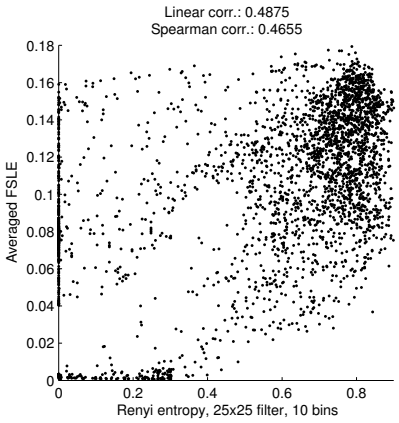


(d) RE vs. FSLE. 25x25 filter.

**Figure 4.9:** Scatter plots for Rényi entropy of various filter sizes versus the FTLE and FSLE. The Lyapunov exponents are averaged with the corresponding filter sizes.

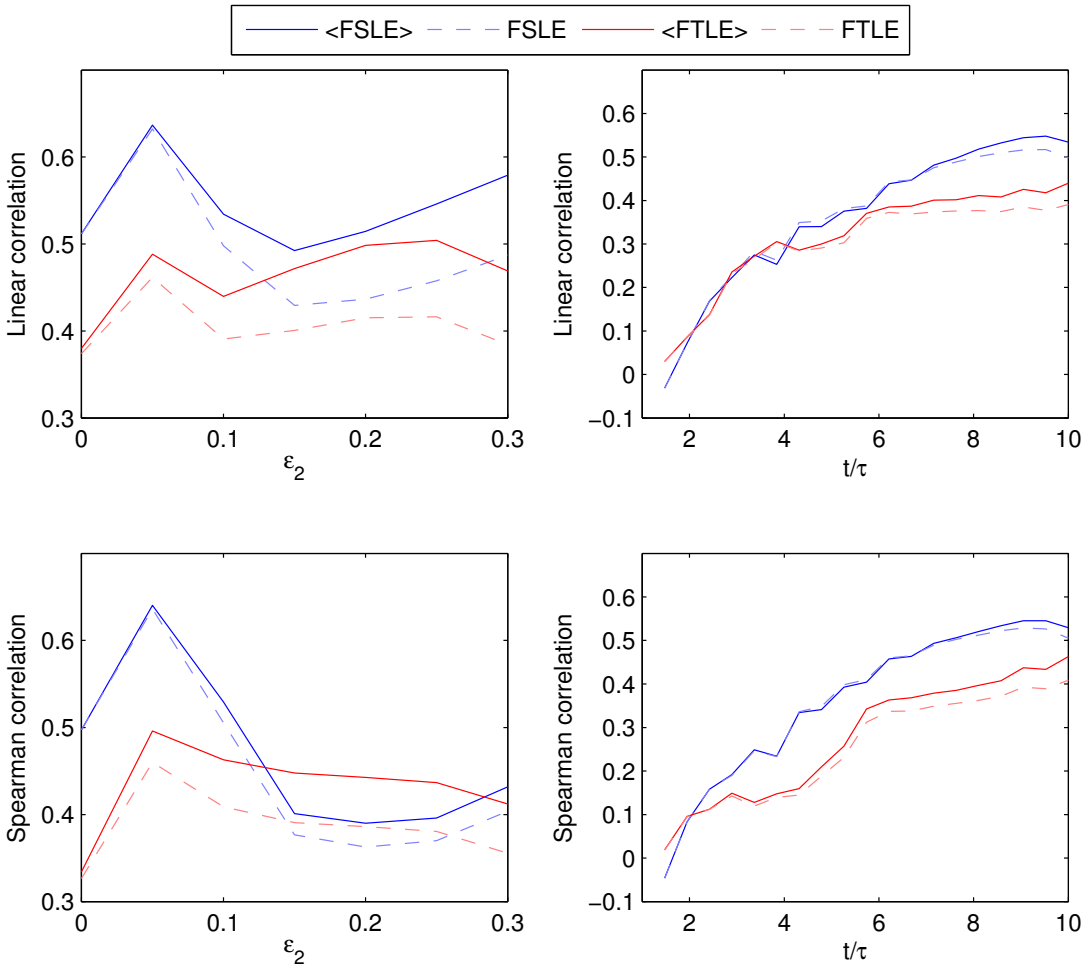


**Figure 4.10:** Linear and Spearman correlation coefficients between Rényi entropy and finite Lyapunov exponents versus $\epsilon_2$ and integration time $t_1$. A 9x9 filter was used. The angled brackets denotes averaged Lyapunov exponents.

# 5

# Discussion

As stated in the introduction, the main goal with this thesis is to examine (1) if the Rényi entropy metric is a valid measure of stratospheric transport and mixing, (2) what conditions must then be fulfilled and (3) what are the possible strengths and weaknesses. With the background and results presented, we are now in position to turn to these questions. Here we would however like to stress that, our method is heuristic in the sense that we try to answer these questions by comparisons between metrics rather then by working from first principles. Our ambition is thus not to give general and definite answers, but to come up with propositions and conditions for its use.

The main focus of the thesis thus lies on the comparison between the Rényi entropy metric and the finite Lyapunov exponents. We start by discussing aspects as dependence on design parameters, particle transport and dependence on the initial tracer field. We then look at correlations to the FTLE and FSLE, followed by our final conclusions. We finish the discussion with some suggestions on further work related to the thesis.

## 5.1 Dependence on design parameters

As previously mentioned, we may identify three parameters which defines the Rényi entropy metric: the number of bins, the filter size and the grid resolution. We may further identify certain restrictions that these parameters impose on the metric.

Perhaps the most obvious restriction is that the grid resolution limits the scale of the filaments observed in the tracer field. If the scale is smaller than the spacing between the grid points, the filament cannot be detected. We may compare this to the length of the initial line segment for the FSLE, although the exact analogy

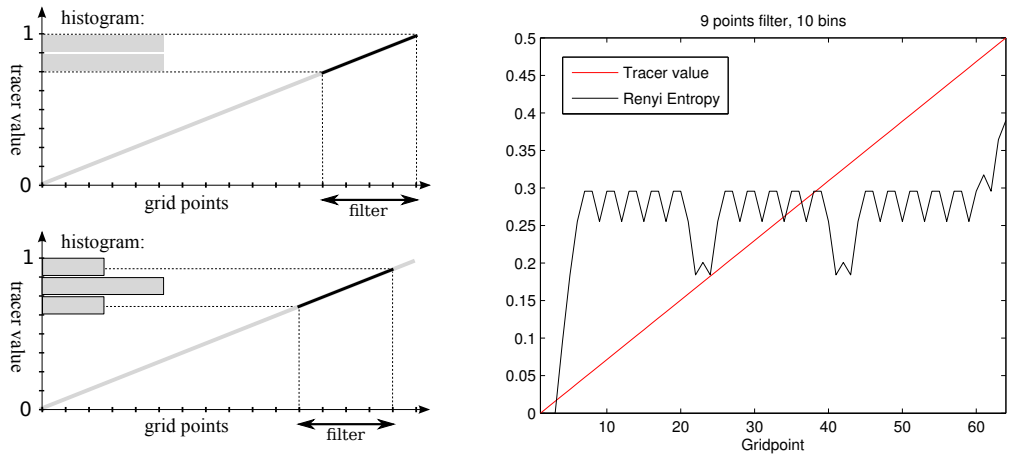


**Figure 5.1:** A linear tracer field being filtered resulting in a inhomogeneous Rényi entropy field. The two plots to the left illustrates that the PDF (or histogram) changes with the position of the filter.To the right, a 9 grid point filter is used with 10 bins resulting in a inhomogeneous entropy field. The inhomogeneity close to the edges of the field is however due to zero padding of the tracer field.

is unclear to us.

Another limitation is due to the discretisation of the tracer field when constructing the probability distributions, which result in a loss of information in the tracer field. In particular, if the scale of the discretised filaments are larger than the filter region, all tracer values ends up in one bin resulting in zero Rényi entropy. Assuming that the act of mixing generates finer and finer filaments in the tracer field, it is natural to also assume that large scale filaments means weak mixing. This could thus set a limit on the weakest amount of mixing possible to observe by the metric. This is further also likely to be the major reason why the correlation coefficients to the FTLE and the FSLE in figure 4.10 are small for short integration times, at which filaments are large in scale. It could possibly also explain why the Rényi entropy appears to deviate more form the FTLE and the FSLE in the upper regions of figure 4.8 and at low values in the scatter plots in figure 4.9.

### 5.1.1 A note on sampling artefacts

We further note a possible problem with the Rényi entropy metric that is related to the number of bins and the filter size. It is likely not major but worth noting. In regions of small gradients in the tracer field, we may identify lines of high Rényi entropy. It is for example seen in the interior of the vortices in figure 4.3. The phenomenon can be illustrated by considering a one dimensional linear tracer field

as illustrated in figure 5.1. We would expect this tracer field to correspond to a homogeneous entropy field, since the local distribution of tracer values is equal over the whole grid. However, if the values for filter regions at different positions do not match up to the same number of bins, the corresponding entropy will not be homogeneous. This is mainly a problem where filament scales are large compared to the filter size, for which the tracer values in the filter region cover a small number of bins. The problem could however probably be handled by anti-aliasing in the probability distribution, although this has not been done here.

## 5.2 Particle transport

The ability to detect particle transport is visualised by comparing the Rényi entropy field with Poincaré sections as shown in figure 4.4. We identify three strong barriers to transport at the boundary to the jet structure, shown as solid lines coloured in blue, red and green. It appears as if the red and blue lines coincide where the Rényi entropy field shows large gradients. There are also weaker barriers within the jet, picked up by the yellow points. These are however not clearly featured in the Rényi entropy field, partly due to the smoothening effect of the filter size.

A quick comparison to the corresponding FTLE and FSLE fields of figure 4.7, indicates that these in fact does not reflect the strong barriers as clearly as the Rényi entropy in this case. The barriers are least clear in the FSLE field, which stretches smoothly over the blue and red barriers.

## 5.3 Dependence on initial tracer field

Since the Rényi entropy metric is based on the tracer field, it is natural to ask in what way the initial tracer field influences the resulting entropy field after advection. It is easy to realise that the initial tracer field must influence the resulting entropy in some extent. For a homogeneous initial tracer field for example, no entropy can ever be produced regardless of mixing. The question is in what extent the initial field affects the Rényi entropy. Figure 4.6 shows the effect of changing from the linear initial tracer field to fields of varying gradients in the latitudinal direction. In contrast to the linear field, these do not have homogeneous Rényi entropy before being advected. When filtering the tracer field after advection, we may then identify a change in entropy either due to mixing or due to initial entropy that has been transported into or out from to the filter regions. The additional effect of transported entropy is likely the reason for the change in the fields shown in figures 4.6(d) and 4.6(e). The change is larger using $C_0(x,y) = \cos(4y - \pi/2)$

as initial tracer field, which is more inhomogeneous in entropy before advection compared to $C_0(x,y) = \cos(y - \pi/2)$.

To fully account for inhomogeneous initial entropy being transported, trajectories are likely needed. The main advantage with the Rényi entropy metric is however that it does not depend on trajectories and such a modification would not be desirable for our use. However, if the mixing is considered in global terms as an average over the whole entropy field, the effect of transported initial entropy should not be a problem.

## 5.4 Rényi entropy versus FTLE and FSLE

Using a linear initial tracer field, we show that the Rényi entropy fields does produce the same structural features as the FTLE and FSLE fields, with a well mixed jet separating the less mixed polar zones from the vortices. The structural similarity is perhaps best seen in the cross-sectional plots in figure 4.8. Overall, we see that the FSLE correlates better to the Rényi entropy than the FTLE in both Spearman and linear correlation coefficients. This could partly be due to the fact that the FSLE depends on the length of the initial line segment in a similar way as to which the Rényi entropy depends on the grid resolution. Both sets a limit on the smallest scale of filaments that can be observed, in contrast to the FTLE which assumes infinitesimal line segments.

The relatively constant relation between correlation coefficients and $\epsilon_2$ in figure 4.10 also suggests that the correlation is not case sensitive. On the other hand, comparing the correlation to integration time we see an increased correlation which levels out after about $t_1 = 6\tau$. This is likely an effect of the filter size being too small compared to the scale of filaments. This is also observed in the regions outside the jet in figure 4.8. The effect can be made smaller either by (a) increasing the number of bins, but with the risk of loosing the shape of the probability distribution, or (b) increasing the filter size, but making the metric less localised.

At the same time as a large filter size seems desirable in terms of covering filaments in the tracer field, we observe that the correlations are higher for the 9x9 filter size than the 25x25 as shown in figure 4.9. The choice of a large filter size does therefore not seem obvious and no clear relation between filter size and correlation is observed. For example, a 15x15 filter size yields a lower correlation than both the 9x9 and the 25x25 filter size. It is however worth noting that, with an increased filter size, both the averaged FTLE and FSLE, as well as the Rényi entropy looses information as they become smoothed. In a sense, the statistics degenerates with an increased filter size and it is thus possible that a more rigorous statistical analysis can be made when comparing correlation coefficients for various filter sizes.

## 5.5 Conclusions

We conclude that the Rényi entropy metric may be related to transport and mixing under the right conditions. We identify these as the following:

1. The grid resolution must be high enough to resolve the filaments in the tracer field.
2. The tracer field must contain gradients.
3. The filter size must be:
   (a) Big enough to cover the fluid filaments.
   (b) Small enough to make the metric localised.
4. The number of bins must be:
   (a) High enough to contain as much information of the tracer field as possible.
   (b) Not too high for a meaningful distribution to be constructed.
5. The initial tracer field should correspond to a homogeneous entropy.

The first condition is perhaps the most obvious, if the resolution is too low, the fluid filaments generated by the mixing cannot be resolved and thus not measured. The second condition just states that we must be able to define material lines to be able to detect the mixing. The third condition state two contradicting requirements on the filter size and should therefore be chosen on a case to case basis. The fourth condition state two, also possibly contradicting, requirements on the number of bins. Here the optimal binning algorithm mentioned previously can be used for choosing the number depending on the tracer values, but a large number of bins is still desirable, especially if the filaments are large in scale. The fifth condition is needed to avoid transported entropy from the initial tracer field, but could possibly be loosened to some extent, depending on the situation. If an average of the Rényi entropy field is calculated such that the mixing is considered as a global scalar quantity, the requirement can be ignored completely. This is also the case if we consider the mixing as an absolute measure, not referring to an initial time. In the latter case, molecular diffusion as well as sources and sinks must however most likely be considered as well.

### 5.5.1 Strengths and weaknesses

We end the assessment of the Rényi entropy metric by identifying its main strengths and weaknesses compared to trajectory based metrics such as the FTLE and the FSLE. We identify the following weaknesses:

- Relationship to physical quantities less clear than FTLE and FSLE.
- Information loss in the tracer field due to discretisation.
- Sensitive to the initial tracer field.

Perhaps the biggest problem with mixing metrics in general is that they are typically not derived from first principles. They can therefore be difficult to relate to physical quantities in terms of fluid dynamics. This also concerns the FTLE and FSLE, although these can be related to average stretching rates (or strain rates as done by for example Pierrehumbert and Yang (1992)), but the exact relation to mixing still appears unclear to us. Another weakness with the Rényi entropy metric is that the tracer field is discretised and a loss of information in the field is unavoidable. This further might set a limit on the weakest level of mixing that the metric can detect. We have further noted that both the bin number and the filter size are ambiguous to some extent and must be chosen on a case to case basis. The last noted weakness is that the metric is dependent on initial tracer field to some degree. An additional point that is not listed is the observed sampling artefacts described above. This is however likely a minor weakness that probably can be avoided by further developing the metric.

We identify the following strengths with the Rényi entropy metric:

+ Independent of velocity fields.
+ Numerically robust.
+ Computationally fast.
+ Easy to implement.

The first point is what motivated the study in the first place, and is the main advantage with the metric. This is of special importance when dealing with real data, where global observations of wind fields usually are associated with larger uncertainties than global observations of tracer fields. The Rényi entropy metric is also numerically robust. Trajectory based metrics rely on solving the velocity field, which can be challenging if the field is chaotic. When dealing with large grids, the third strength is also of importance. We find that, given a tracer field, the Rényi entropy metric can be up to about 3 orders of magnitudes faster in computation

time than the FTLE and FSLE, depending on integration time and error tolerance of the trajectory solver. Finally, the metric is essentially an image filter and the implementation is fairly straight forward.

## 5.6 Further work

We end the thesis with some suggestions on further work. Due to the limited time frame, there are obviously a number of aspects and questions that we have not considered. First of all, there are a number of physical aspects that could be included in the study. The effect of diffusion would for example be interesting to study and of importance if the metric is applied on real data over long time scales or on small spatial scales. Another aspect is the effect of sources and sinks in the tracer field which also could be of concern for long time scales.

There are further a number of ways the Rényi entropy metric could be improved. First of all, a solution to the sampling artefacts noted above would be desirable. One solution could possibly be based anti-aliasing in the histogram.

To make the choice of filter size less ambiguous, it would also be interesting to look at the effects of scaling of the filter size. For example, one method of measuring global mixing in tracer fields that has not been considered here utilises the so called *box counting dimension* (Ott, 2002) of material lines. Perhaps an analogy of this fractal dimension could be made for the Rényi entropy metric, for which the scaling of the Rényi entropy with filter size could be examined. Other ways of incorporating multiple filter sizes into one measure could probably be studied as well. After all, mixing often results in fractal structures in the tracer field, which in turn relates to scaling.

Finally, we recognise that the approach of this thesis is heuristic. We have not worked from first principles and the conclusions are thus based on comparisons rather than rigorous derivations. In order to fully understand the relationship between the Rényi entropy, transport and mixing, a more rigorous and theoretical approach is probably needed. This would be useful in order to further relate the Rényi entropy metric to physical quantities in terms of fluid dynamics as well.

# Bibliography


Andrews, D., Holton, J. and Leovy, C. (1987), *Middle atmosphere dynamics*, International geophysics series, Academic Press.

Aurell, E., Boffetta, G., Crisanti, A., Paladin, G. and Vulpiani, A. (1997), 'Predictability in the large: an extension of the concept of lyapunov exponent', *Journal of Physics A: Mathematical and General* **30**(1), 1–26.

Boffetta, G., Lacorata, G., Redaelli, G. and Vulpiani, A. (2001), Detecting barriers to transport: A review of different techniques, Technical Report 1-2.

Bowman, K. P. (1993), 'Large-scale isentropic mixing properties of the antarctic polar vortex from analyzed winds', *Journal of Geophysical Research* **98**(D12), 23,013–23,027.

Camesasca, M., Kaufman, M. and Manas-Slaczower, I. (2006), 'Quantifying fluid mixing with the shannon entropy', *Macromolecular Theory and Simulations* **15**(8), 595–607.

Eckmann, J. and Ruelle, D. (1985), 'Ergodic theory of chaos and strange attractors', *Rev. Mod. Phys.* **57**, 617–656.

Garny, H., Bodeker, G. E. and Dameris, M. (2007), 'Trends and variability in stratospheric mixing: 1979–2005', *Atmospheric Chemistry and Physics* **7**(3), 5611–5624.

Geist, K., Parlitz, U. and Lauterborn, W. (1990), 'Comparison of different methods for computing lyapunov exponents', *Progress of Theoretical Physics* **83**(5), 875–893.

Guida, A., Nienow, A. W. and Barigou, M. (2010), 'Shannon entropy for local and global description of mixing by lagrangian particle tracking', *Chemical Engineering Science* **65**(10), 2865–2883.

Haynes, P. (2005), 'Stratospheric dynamics', *Annual Review of Fluid Mechanics* **37**, 263–293.

Haynes, P. and Shuckburgh, E. (2000), 'Effective diffusivity as a diagnostic of atmospheric transport - 1. stratosphere', *J. Geophys. Res* **105**(D18), 22777–22794.

Krützmann, N. C., McDonald, A. J. and George, S. E. (2008), 'Identification of mixing barriers in chemistry-climate model simulations using rényi entropy', *Geophysical Research Letters* **35**(L0), 6806–6811.

McKenna, D. S., Konopka, P., Grooss, J. U., Günther, G., Müller, R., Spang, R., Offermann, D. and Orsolini, Y. (2000), 'A new chemical lagrangian model of the stratosphere (clams). 1. formulation of advection and mixing', *Journal of Geophysical Research* **107**(D16), 4309.

Nakamura, N. (1996), 'Two-dimensional mixing, edge formation and permeability diagnosed in area coordinates', *J. Atmos. Sci* **53**, 1524–1537.

Oseledets, V. I. (1968), 'A multiplicative ergodic theorem: Characteristic lyapunov exponents of dynamical systems', *Transactions of Moscow Mathematical Society* **19**, 197–231.

Ott, E. (2002), *Chaos in dynamical systems*, Cambridge University Press.

Ottino, J. M. (1989), *The Kinematics of Mixing: Stretching, Chaos and Transport*, Camebridge University Press.

Pierrehumbert, R. T. and Yang, H. (1992), 'Global chaotic mixing on isentropic surfaces', *Journal of the Atmospheric Sciences* **50**(15), 2462–2480.

Plumb, R. A. (1996), 'A " tropical pipe" model of stratospheric transport', *Journal of Geophysical Research* **101**(D2).

Renyi, A. (1960), On measures of entropy and information, *in* 'Berkeley Symposium Mathematics, Statistics, and Probability', pp. 547–561.

Shannon, C. E. (1948), 'A mathematical theory of communication', *Bell system technical journal* **27**, 417–436 and 623–656.

Shepherd, T., J.N., K. and Ngan, K. (2000), 'On the nature of large-scale mixing in the stratosphere and mesosphere', *JOURNAL OF GEOPHYSICAL RESEARCH* **105**(D10), 12433–12446.

Shuckburgh, E. and Haynes, P. (2003), 'Diagnosing transport and mixing using a tracer-based coordinate system', *Physics of Fluids* **15**(11), 3342–3357.

*SPARC Report No. 5* (2010), *in* 'SPARC CCMVal', SPARC CCMVal Group.

Sparling, L. C. (2000), 'Statistical perspectives on stratospheric transport', *Reviews of Geophysics* **38**(3), 417–436.

Wallace, J. and Hobbs, P. (2006), *Atmospheric Science: An Introductory Survey*, International Geophysics Series, Elsevier Academic Press.

Wolf, A., Swift, J. B., Swinney, H. L. and Vastano, J. A. (1985), 'Determining lyapunov exponents from a time series', *Physica* **D**, 285–317.

# A

# Appendix

## A.1 CLE expressed in terms of $r_{ii}$

We now show that the CLE can be expressed in terms of the diagonal elements of the right triangular matrix $\mathbf{R}$. Consider the tangent matrix in eq. 2.15 and note that we can write:

$$\lambda_i(\mathbf{x}_0) = \lim_{t\to\infty} \lim_{|\delta\mathbf{x}_{0i}|\to 0} \frac{1}{t} \ln\left(\frac{|\mathbf{T}\delta\mathbf{x}_{0i}|}{|\delta\mathbf{x}_{0i}|}\right) = \lim_{t\to\infty} \frac{1}{t} \ln\left(|\mathbf{T}\hat{\mathbf{v}}_{0i}|\right)$$

where $\hat{\mathbf{v}}_{0i} = \delta\mathbf{x}_{0i}/|\delta\mathbf{x}_{0i}|$. The limit as the initial displacement goes to zero now has been made implicit by assuming that the linearisation is valid. We can factorise the tangent matrix by QR factorisation and note the following:

$$\begin{aligned} |\mathbf{T}\hat{\mathbf{v}}_{0i}| &= (\hat{\mathbf{v}}_{0i}^{tr}\mathbf{T}^{tr}\mathbf{T}\hat{\mathbf{v}}_{0i})^{1/2} = \\ &= (\hat{\mathbf{v}}_{0i}^{tr}\mathbf{R}^{tr}\underbrace{\mathbf{Q}^{tr}\mathbf{Q}}_{\equiv\mathbf{I}}\mathbf{R}\hat{\mathbf{v}}_{0i})^{1/2} = |\mathbf{R}\hat{\mathbf{v}}_{0i}| \end{aligned}$$

That is, if we let $\hat{\mathbf{v}}_{0\,1} = [1,0]$ and $\hat{\mathbf{v}}_{0\,2} = [0,1]$, we can write the exponents as:

$$\lambda_i(\mathbf{x}_0) = \lim_{t\to\infty} \frac{1}{t} \ln\left(|R_{ii}|\right)$$

That is, as in eq. 2.18.